ACS OMEGA

Open Access



http://pubs.acs.org/journal/acsodf

Article

# Topological Characteristics of the Pore Network in the Tight Sandstone Using Persistent Homology

Wei Wang,* Zhiyong Yan, Lina Wang, and Shuang Xu

Cite This: *ACS Omega* 2024, 9, 11589–11596

Read Online

ACCESS | Metrics & More | Article Recommendations | Supporting Information

**ABSTRACT:** Tight sandstone reservoirs have become important areas for unconventional reservoir development, and their pore network is a key feature for identifying tight sandstone, which affects fluid migration path and reservoir development efficiency. However, the connectivity characteristics of the pore network at different scales have remained unclear owing to the numerous pores and uneven pore shape. Here, using pore size distributions from many hundreds of tight sandstone samples and subsequent topological data analysis, we construct the topological structure of the pore network in the Yanchang Formation tight sandstone of the Ordos Basin in China and visualize the topological characteristics of the pore network with distances. We show that there are three connected groups within the pore structure of the tight sandstone. The topology of the pore network resides on a trident ring manifold, suggesting that the pore network in the tight sandstone encompasses three obvious dominant connection paths. One prominent bar on the $H^0$ dimension in the barcode indicates a two-point connection from nanoscale to microscale in the pore network. Three prominent bars with varying durations on the $H^1$ dimension indicate the presence of three separate multipoint connections within a limited extent in the pore network. Connectivity of combined pores is good and controlled by the topological structure of the pore network. This demonstration of pore connections on a trident ring manifold provides a population-level visualization of the pore network in the tight sandstone.

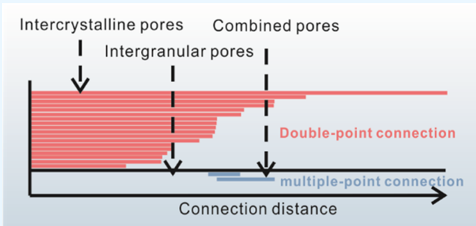


## 1. INTRODUCTION

With the advancement of exploration technologies and the depletion of conventional oil reserves, there has been a growing global focus on tight sandstone reservoirs for oil and gas exploration.[1,2] The pore network of tight sandstones exhibits a remarkable level of dynamism and intricacy, and understanding the connectivity of tight sandstone reservoirs is crucial for diffusion, migration, and even fluid−rock reactions of $CO_2$ in tight sandstone reservoirs.[3,4] In recent years, scholars have conducted various experiments, such as rate-controlled porosimetry, low-pressure gas adsorption, scanning electron microscopy (SEM), X-ray-computed tomography, high-pressure porosimetry (HIP), nuclear magnetic resonance, and small-angle and ultrasmall-angle neutron scattering to study the pore structure and connectivity characteristics of tight sandstones. These studies have yielded valuable parameters, including pore size distribution, pore−throat ratio, movable fluid, pore shapes, and connectivity.[5−11] However, analyzing the pore network in tight sandstone requires treating the pore network as a complex interconnected system. Each pore is considered a node, and a topological structure is established based on the interconnections between these pores. By expanding the pore radius, the relationship between adjacent pores changes. The larger the connect radius, the greater the connectivity distance between pores and the larger the distribution scale of the pore network it forms. With hundreds of thousands of micropores and multidimensional data represented by connections between pore throats, detecting changes in pore connections can be challenging due to the dynamic and complex nature of pore networks.[12] Therefore, it is crucial to employ stable and intuitive methods for quantifying and visualizing the pore network of tight sandstone reservoirs.

Persistent (co)homology is a powerful tool in the field of topological data analysis (TDA), which has shown success in various domains.[13] It has been employed in the analysis of neural data and their topology,[14−16] molecular representation schemes,[17] identification of warning signals for financial crises,[18] analysis of powder compacts,[19] and the study of a complex and dynamical system.[20,21] In the study by Ando et al., 4D-CT scanning and persistent homology were utilized to analyze the pore connection mechanism in the duct structure of pure iron. This approach allowed them to predict and quantify changes in pore connection, demonstrating the application of persistent homology in studying the pore network.[22] These diverse applications highlight the versatility of persistent homology in capturing and analyzing the

**Received:** November 7, 2023
**Revised:** January 12, 2024
**Accepted:** February 13, 2024
**Published:** February 26, 2024

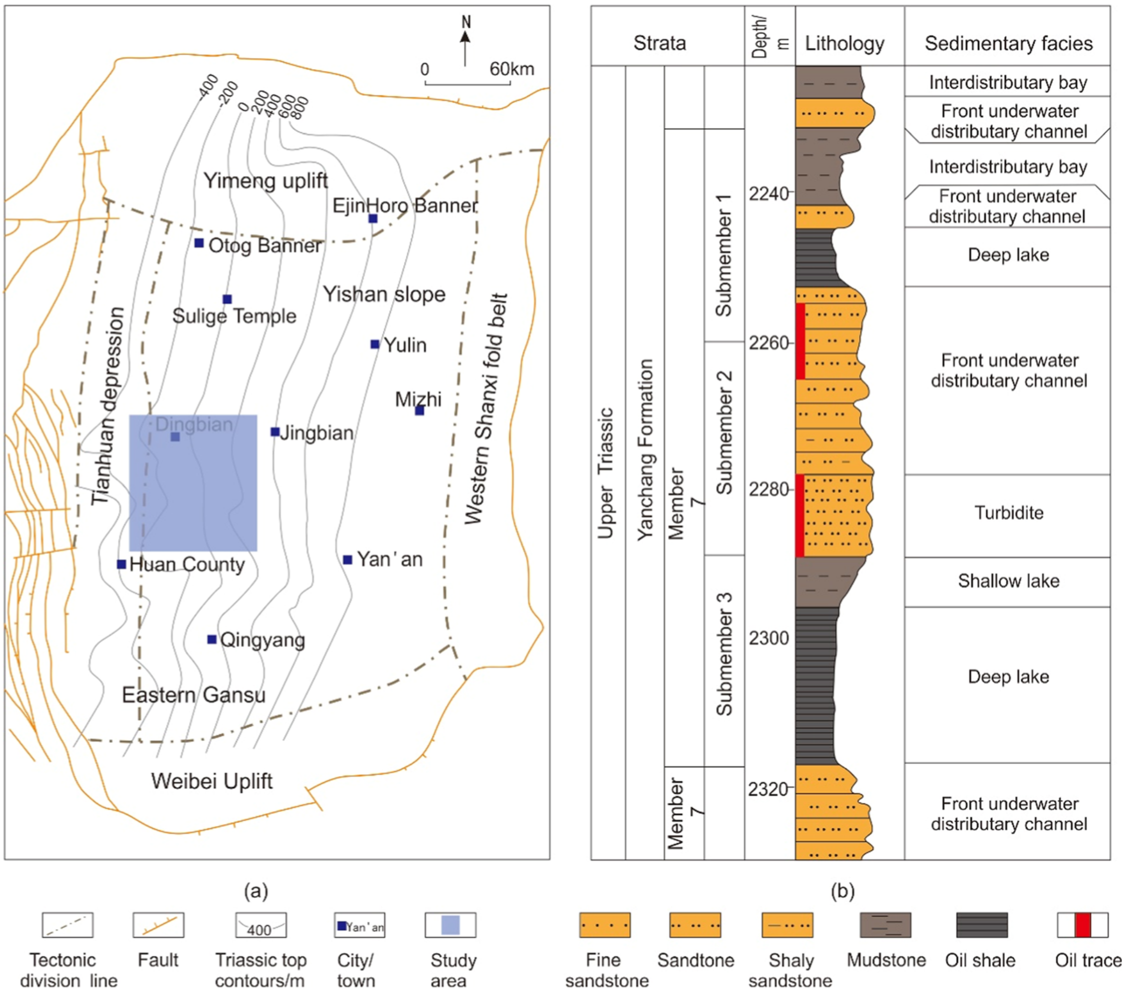


**Figure 1.** Geological and lithological features of the Ordos Basin. (a) Location and tectonic units of the research area. (b) Stratigraphic column of the Chang 7 Formation.

topological features and structures present in different data sets.

In this study, we used persistent homology to provide a quantitative framework for depicting the topological structure of the pore network. We aim to determine the pore network of different scales and track the changes in pore connectivity of the tight sandstone with distance.

## 2. METHOD

**2.1. Samples.** For this investigation, samples of the tight sandstone were collected from the Chang 7 Member of the Triassic Yanchang Formation in the Ordos Basin of China (Figure 1A). The Chang 7 subsection was characterized by semideep and deep lake conditions, which led to the development of tight sandstone formations near the source rocks (Figure 1B).

A total of 120 cylindrical core plugs with a diameter of 2.5 cm were drilled in alignment with the bedding surface of the tight sandstone. After removing residuals, the samples underwent a 24 h vacuum drying process at a temperature of 105 °C. Subsequently, each sample was subjected to helium porosity and nitrogen permeability tests, as well as HIP tests. Eight additional samples were collected for thin section and SEM analysis.

**2.2. Experimental Section.** *2.2.1. Thin Section and SEM Analysis.* In the initial stage, we impregnated thin sections of tight sandstones with colored epoxy to visualize the pore system. This technique allowed for the depiction of the pore spaces within the rock. Subsequently, we examined these impregnated thin sections to analyze the characteristics of the pores and detrital components present in the tight sandstone. To further investigate the samples, we performed scanning electron microscopy (SEM) measurements. The samples were coated with a layer of gold, which enhanced the contrast and provided better resolution during imaging. The SEM analysis enabled the detection and characterization of various features, including the cementation and microscopic characteristics of tight sandstones.

*2.2.2. High-Pressure Porosimetry (HIP).* In this study, we used an Autopore 9420 mercury porosimeter to conduct HIP tests on tight sandstone samples with a maximum displacement pressure of 200 MPa. By analyzing the pressure data and corresponding mercury saturation, intrusion curves were obtained. It is important to note that the capillary pressure curve serves as an indicator of the pore structure as the size and connectivity of the pores influence capillary pressure. The pore diameter was evaluated using the Washburn equation, as shown in eq 1.[23]

$$d = \frac{2\gamma \cos \theta}{P} \quad (1)$$

where $d$ represents the pore radius in $\mu$m, $P$ is the capillary pressure in MPa, $\gamma$ is the surface tension of the mercury with 480 dyn/cm, and $\theta$ is the contact angle between mercury and the solid surface with 140°.

**2.3. Data Set.** During the mercury intrusion process, the entry of mercury into the pores of tight sandstones provides valuable insights into the pore network. The resulting mercury intrusion curves obtained from the samples can be transformed into pore size distribution curves. In these curves, the observation is the pore radius, while the variables are the distribution frequency.

To investigate and analyze the topology of the pore network, we developed a multidimensional pore size distribution module using 120 samples. This module comprises a matrix with 120 rows and 20 columns (Supporting Table 1). The column data represent the pore radius, ranging from 0.0037 to 25.3156 $\mu$m, with a total of 20 values. The row data corresponds to the frequency values of the pores in each sample

**2.4. Analysis of the Connection between Pores by Persistent Homology.** *2.4.1. Data Dimensionality Reduction.* Dimensionality reduction techniques enable the transformation of high-dimensional data into a lower-dimensional space, facilitating the analysis and visualization of the pore network in tight sandstone reservoirs.[24]

Principal component analysis (PCA) identifies the most important patterns and variations in the data by creating new variables, called principal components, that are linear combinations of the original variables. The principal components that capture the largest amount of variance in the data set were retained for further analysis.

The uniform manifold approximation and projection (UMAP) algorithm has proven to be effective in processing data sets that contain noise and outliers while preserving important structural features. By utilizing UMAP for dimensionality reduction, the visualization and analysis of the topological structure in point cloud data can be improved and topological differences across different data sets can be compared.[25]

To construct the initial high-dimensional graph, UMAP introduces the concept of a "fuzzy simple complex". This concept represents a weighted graph, in which the edge weights indicate the likelihood of connecting two points. UMAP determines connectivity by extending a radius from each point and establishing connections when these radii overlap.[26] Furthermore, UMAP ensures a balance between local and global pore connections by specifying that each point must be connected to its nearest neighbor. This constraint helps to preserve both local and global relationships within the pore structure. Overall, UMAP offers a powerful approach to dimensionality reduction and visualization, enabling the exploration and understanding of complex pore networks with noisy and outlier-prone characteristics.

The resulting curves were smoothed using a Gaussian kernel with $\sigma = 2$ bins and then standardized ("$z$-scored"). We used a two-stage dimensionality reduction procedure on the matrix of the pore size distribution. In the first stage, we applied PCA to reduce the dimension of the matrix (pore radii as observations and frequency as variables), and the principal components were retained. In the second stage, we ran UMAP on the principal components. Several hyperparameters were specified for the UMAP algorithm. The "n_dims" parameter was set to 3, indicating that the dimensionality of the projected data was reduced to three dimensions. The random-state parameter was set to 42, ensuring reproducibility of the results. The "metric" parameter was set to "euclidean", indicating that the Euclidean distance was used to measure the similarity between data points. The "n_neighbors" parameter was set to 10, specifying the number of neighboring points considered during the optimization process. Finally, the "min_dist" parameter was set to 0.1, controlling the minimum distance between points in the low-dimensional projection.

*2.4.2. Persistent Homology.* Persistent homology, a tool in topological data analysis, is used to characterize the underlying connectivity features of a data set. These features can be understood as connected components, loops, voids, and higher-dimensional structures. The algorithm in persistent homology gradually expands spheres around each point in the point cloud. As these spheres expand uniformly, they capture the local connectivity information on the data set. In the context of persistent homology, the lifetime of these features is taken into account.[16,27] By combining the spheres at a specific radius, a space is formed with various types of voids, including zero-dimensional (0D) connected components, one-dimensional (1D) loops, two-dimensional (2D) voids, and higher-dimensional features (Figure 2). By increasing this radius from zero until all of the balls intersect, we observe the lifetime of each hole—the range of radii from when the hole first appears until it disappears. These lifespans are visually represented as bars, and the complete set of bars is referred to as the barcode.[14] The filtration parameter or proximity parameter refers to a value that determines the scale or threshold at which the data is analyzed. At each step of the filtration, the topological features are computed and tracked as they appear, merge, or disappear. The persistence barcode or diagram visualizes this evolution by representing each feature as an interval, where the length of the interval signifies the persistence or robustness of that feature. The filtration

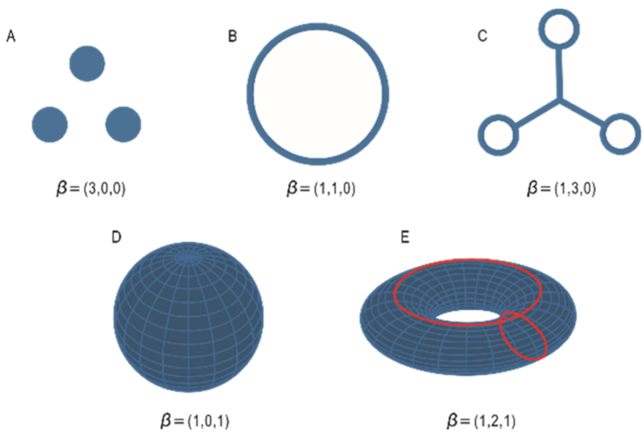


**Figure 2.** Schematic diagram illustrating the homology topological space based on the number of topological holes ($\beta$). (A) Three disks, which has a 0D hole (a connected component). (B) A circle has a 0D hole and a 1D hole. (C) A trident ring has a 0D hole and three 1D holes. (D) A sphere is a connected component and has a 2D hole (a cavity). (E) A torus is a connected component with two 1D holes (illustrated with red circles) and one 2D hole (a cavity in the interior of the torus).

parameter influences which features are detected and how they are represented in the barcode. Choosing an appropriate filtration parameter is crucial for capturing the desired topological information in the data.

*2.4.3. Analysis of the Connection between Pores by Persistent Homology.* Persistent homology summarizes the topological features of data. The lifetime of pore connections can be defined by the process of expanding the pore radius from the initial appearance of the pore to the radial interval filled. As the sphere's radius increases, the interpore distance gradually widens. According to the length of bars in the barcode, the lifetime of each pore connection of zero-dimensional ($H^0$), one-dimensional ($H^1$), and two-dimensional ($H^2$) in the pore distribution matrix can be represented (Figure 3). Short bars are considered noise, while significantly longer bars signify crucial topological information within the point cloud. Bar length denotes the birth and death times of pore-connected structures. A greater difference between birth and death times implies an extended duration for the corresponding pore connection.

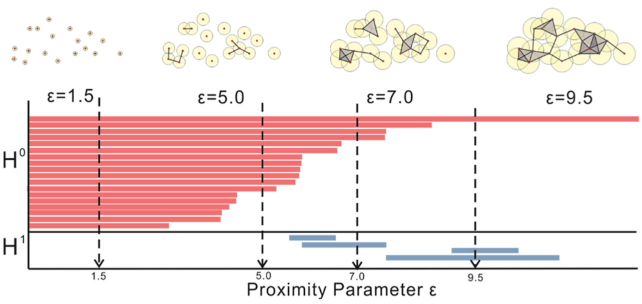


**Figure 3.** Schematic diagram of barcodes with persistent homology. The lifetime of each hole of dimension zero ($H^0$), one ($H^1$), and two ($H^1$) is indicated by the length of the bar in the barcode diagram. Each node in the diagram represents a pore, and each edge represents a connection. The $\varepsilon$ denotes an increase in the distance between the connected pores.

In persistent homology, the 0D persistence features represent connected components, the 1D persistence features correspond to tunnels or loops, and the 2D persistence features correspond to cavities. In three-dimensional space, the barcodes of $H^0$, $H^1$, and $H^2$, respectively, represent configurations for two-point connections, polygons formed by more than three-point connections, and polygons formed by more than four points.[22] A model for the pore network has been proposed for tight sandstones. Therefore, in this study, the pores were considered point clouds, and the barcode was applied to quantitatively analyze their pore network.

## 3. RESULTS

**3.1. Petrology Characteristics of Samples.** The Chang 7 tight sandstone is composed mainly of feldspathic lithic sandstone (Figure 4A). The primary rock components are feldspar and quartz, with rock fragments present, as well. The cementing materials primarily consist of authigenic clay minerals, such as chlorite, kaolinite, and Illite, as well as carbonate (Figure 4B,C).

The predominant pore types in the tight sandstone include intergranular, dissolution, intercrystalline, and combined pores. Intergranular pores are primary space that persists after compaction and cementation (Figure 4D). Dissolution pores are formed through the dissolution of mineral grains (Figure 4D). Through this dissolution process, these pores can connect with other pores, leading to the development of combined pores with large radii (Figure 4E). Intercrystalline pores are developed in clay minerals (Figure 4F).

The porosity of the 120 samples ranges from 5.9 to 13.1%, averaging at 10.2%. Meanwhile, their permeability ranges between $0.04 \times 10^{-3}$ and $0.65 \times 10^{-3}$ $\mu m^2$, with an average permeability of $0.24 \times 10^{-3}$ $\mu m^2$ (Supporting Table 2). The correlation between permeability and porosity is weak ($R^2$ = 0.21), indicating that the permeability is not dependent on the total pore space in samples but rather is influenced by the connectivity and distribution of pores (Figure 5).

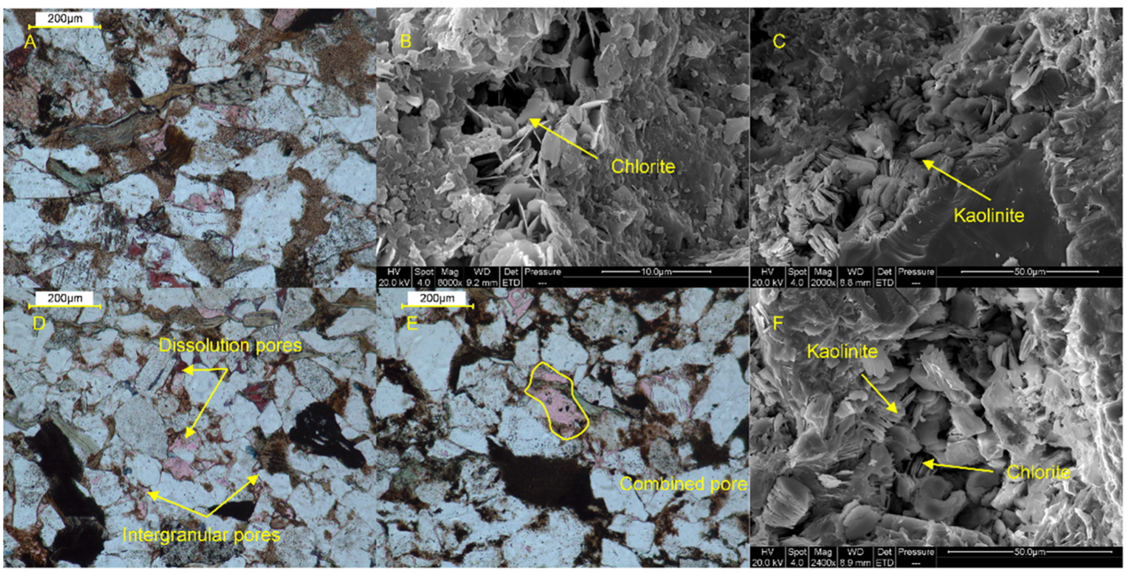


**Figure 4.** Petrophysical characteristics of tight sandstone samples. (A) Feldspathic lithic sandstone in sample FT-1. (B) Chlorite in sample FT-2. (C) Kaolinite in sample G4. (D) Intergranular pores and dissolution pores were isolatedly distributed in sample FT-6. (E) Combined pores with large radius in sample FT-4. (F) Intercrystalline pores in chlorite in sample FT-7.


https://doi.org/10.1021/acsomega.3c08847
ACS Omega 2024, 9, 11589−11596

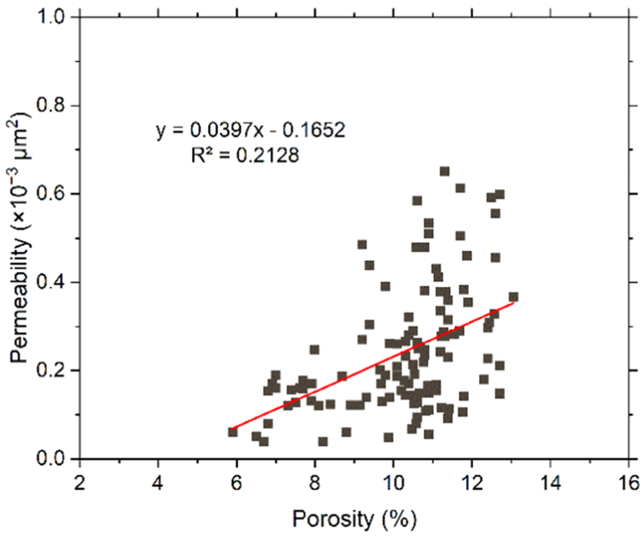


**Figure 5.** Porosity vs permeability of samples.

### 3.2. Data Dimensionality Reduction.

*3.2.1. PCA.* According to the PCA results, the variance explained by the 20 principal components (PCs) was examined. The cumulative variance contribution rate of the initial six principal components accounts for 99.9%, signifying that they account for a significant proportion of the variance within the data set (Figure 6). Thus, the first six PCs have been retained.

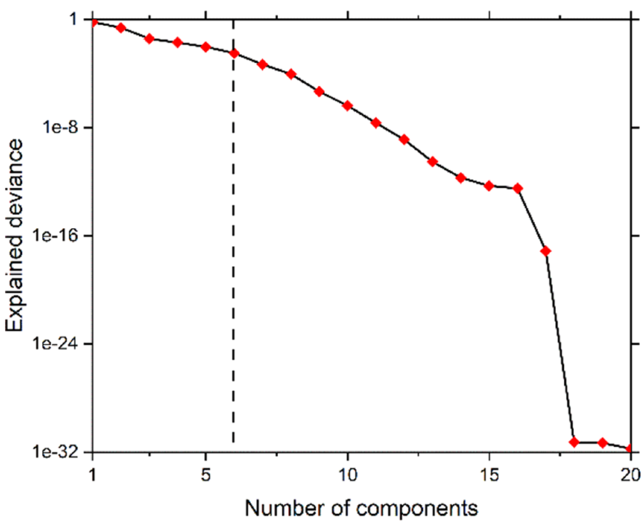


**Figure 6.** Variance explained by the 20 principal components (PCs) after applying PCA to the data set. A noticeable decrease after the sixth PC.

*3.2.2. UMAP.* UMAP was used to reduce the six principal components into a 3D visualization (Figure 7). The resulting scatter plot exhibited a distinctive finger-like structure, indicating a layered configuration in the connectivity of pores.[15,16] The connectivity between pores is generally weak, with most of the pores being connected from a single node. In the 3D visualization, three distinct clusters of closely related data points were identified, suggesting the presence of three connected groups within the data.

### 3.3. Pore Network by Persistent Homology.

Persistent homology analyses were used to construct barcodes for the data set. In the analysis, four long-lived bars were detected, including a single 0D hole represented by a $H^0$ bar and three 1D holes represented by $H^1$ bars (Figure 8). These bars exhibited significantly longer lifetimes compared to other bars. This observation suggests that the network dynamics during HIP exist on a low-dimensional manifold.

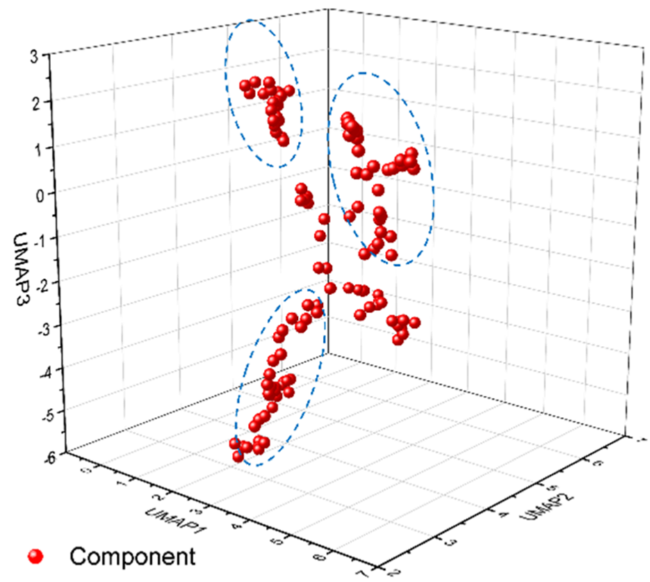


**Figure 7.** 3D visualization of the data set after UMAP. Three distinct clusters of closely related data points were seen.

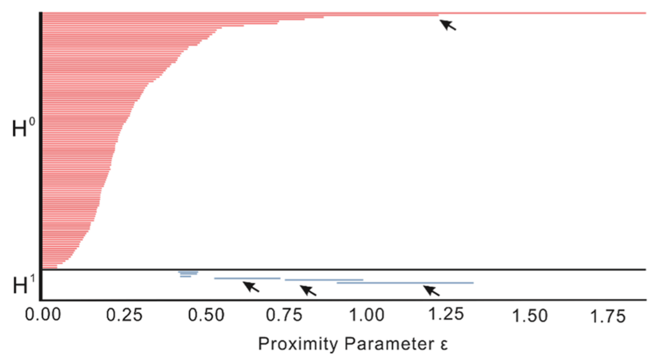


**Figure 8.** Barcode diagram of the data set of samples, indicating four most prominent bars across all dimensions (one prominent bar in dimension 0 and three in dimension 1).

## 4. DISCUSSION

### 4.1. Connections between Pores by Persistent Homology.

In the analysis of persistent homology, each pore corresponds to a node, while each connection corresponds to an edge. Barcodes can be utilized to observe and analyze the structural characteristics, aggregation, and connectivity among various regions of the pore network in tight sandstone. A $H^0$ bar in the barcode signifies a homological feature that spans the entire scale. Three $H^1$ bars in the barcode indicate the existence of three homological features in one dimension. Each $H^1$ bar represents a one-dimensional homological feature, with its horizontal direction denoting the range of the pore radius wherein the feature appears. The presence of three $H^1$ bars with varying durations suggests that these one-dimensional homological features exist within distinct pore ranges, highlighting the existence of


https://doi.org/10.1021/acsomega.3c08847
ACS Omega 2024, 9, 11589−11596

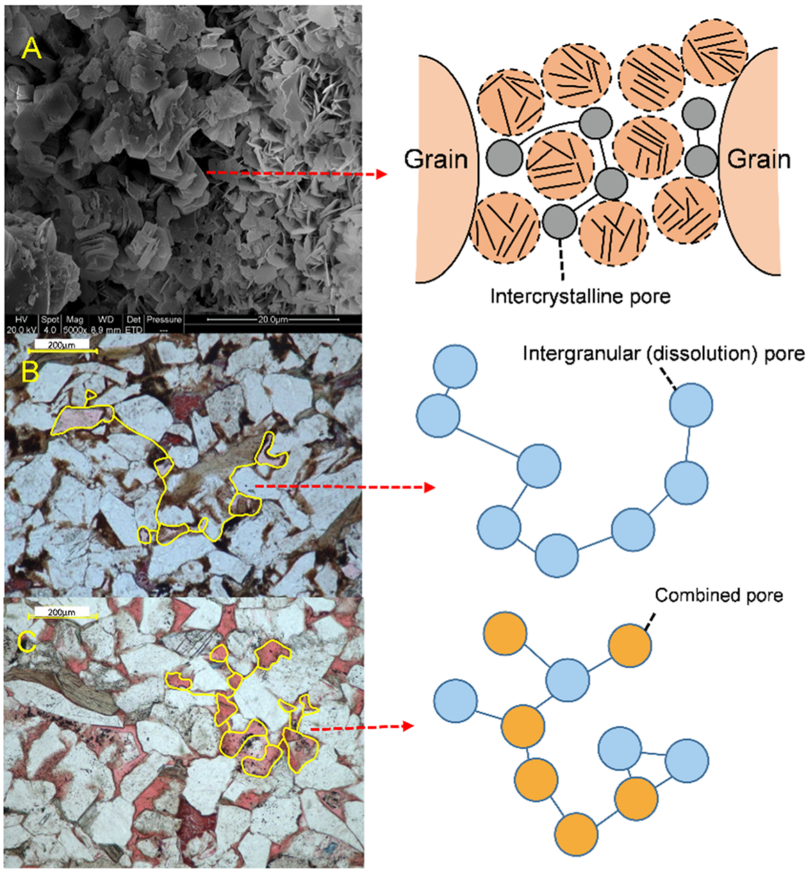


**Figure 9.** Schematic diagrams of the pore connection. (A) Adjacently developed intercrystalline pores and their connected paths, sample FT-5. (B) Isolated intergranular (dissolution) pores and their connecting paths, sample FT-2. (C) Combined pores and their multiple connecting paths, sample FT-3.

multilevel pore structures within the tight sandstone. The barcodes clearly exhibit characteristics resembling a trident ring, which possess a hollow area (0D hole) connected to it via three different paths or channels (1D hole). This suggests that the pore network in the tight sandstone encompasses three distinct connection paths.

Through quantitative analysis of the connectivity in the tight sandstone, the $H^0$ bar signifies the presence of a double-point connection that spans the entire pore network. Although the pore structure of tight sandstones is connected, its connectivity is poor. The $H^1$ bar indicates the existence of a multipoint connection structure within the pore network, which forms a polygon by connecting more than three points. Three $H^1$ bars with varying durations indicate the existence of three obvious pore networks with good connectivity. However, these three $H^1$ bars are not synchronized and are short-lived, suggesting that these three network channels can only exist within a small range and are not interconnected with each other.

**4.2. Influence of Diagenesis on Pore Network.** The tight sandstones are characterized by three distinct pore types with different fractal dimensions and corresponding pore structures: combined pores, isolated grain pores, and clay-dominated pores.[28] The pore spaces of these three types gradually transition from the microscale to the nanoscale. Combined pores are formed by dissolution pores that connect with surrounding pores and are easily identified by their irregular shape. These pores have multidirectional connected paths, leading to a better connectivity. Isolated grain pores have a limited number of poorly connected paths, resulting in a weak connectivity. Clay-dominated pores, on the other hand, have narrow and complex connected paths, leading to poor connectivity.

Intercrystalline pores are widely distributed in authigenic clay, and they are adjacent to each other but have poor connectivity, with most of them being unidirectional connections (Figure 9A). As a result, in the low $\varepsilon$ area of the barcode, one bar exists on $H^0$ while no bar appears on $H^1$.

Both intergranular pores and dissolution pores have larger radii. However, significant compaction and cementation effects cause the throats between particles to narrow, resulting in poor interconnectivity among intergranular pores. Similarly, dissolution pores, which are primarily formed within particles through the dissolution of acidic fluid, also display poor connectivity. Additionally, there is poor connectivity between intergranular pores and dissolution pores (Figure 9B). Consequently, in the high $\varepsilon$ area of the barcode, one bar exists on $H^0$ while no long bar appears on $H^1$.

Moreover, intercrystalline pores provide a connecting channel for dispersed intergranular pores and dissolution pores, and these pores construct a multiscale pore network.[29] Therefore, a $H^0$ bar exists from low $\varepsilon$ values to high $\varepsilon$ values, indicating that there is a pore network with poor connectivity ranging from nanoscale to microscale in the tight sandstone.

After strong dissolution, the dissolution pores connect with adjacent pores, forming combined pores. The combined pores can be connected to the surrounding pores with good connectivity, showing a clear $H^1$ bar in the barcode (Figure 9C). However, due to the low content and dispersed


https://doi.org/10.1021/acsomega.3c08847
ACS Omega 2024, 9, 11589−11596

distribution of combined pores, it is not possible to stably form a multiconnected pore network on a large scale. It can only form a multipoint connected network within a small range. Therefore, combined pores can enhance the local connectivity of pores, leading to only a few $H^1$ bars with varying durations in the barcode.

Through diagnostic processes, the tight sandstone undergoes changes in its pore structure, leading to the formation of distinct pores with varying radii and connectivity. These include intercrystalline pores, dissolution pores, intergranular pores, and combined pores. These interconnected pores create a complex, multilevel pore network. By analyzing the modifications in the pore network across different scales, we can gain a comprehensive understanding of the flow paths within tight sandstone.

During compaction, the pore is reduced, causing the pores to become isolated and the connectivity between pore throats to deteriorate. Quartz and calcite cements fill the pore−throat space, thereby impacting the quality of the reservoir. Additionally, clay minerals divide intergranular pores into intricate seepage pathways, hindering the movement of clay-bound water on the surface of intercrystalline pores. Consequently, fluid flow through pore throats is impeded, and the effective storage capacity of the pores is diminished. After intensive dissolution, dissolution pores could connect with other pores to form irregular combined pores with a large storage space, resulting in good connectivity between dissolution pores and dissolution throats.

Thus, pores with good local connectivity will become objectively dominant connecting paths, which can affect the oil charging area and development efficiency.

## 5. CONCLUSIONS

A combination of cast thin sections, SEM, HIP, and persistent homology was conducted to visualize and quantify the topological structure of the network in the tight sandstone and their influencing factors. The following conclusions were derived:

1. The population-level characteristics of the pore network in the tight sandstone can be visualized and quantified using the lifetime of the bar in the barcode, and the connectivity changed with increasing pore distance.
2. The topology of the pore network resides on a trident ring manifold, consisting of one bar on the $H^0$ dimension and three bars on the $H^1$ dimension of the barcode.
3. Connectivity of combined pores is good, and connectivity of tight sandstones is controlled by pore−throat structures formed by dissolution.
4. The pore network in the tight sandstone encompasses three highly connected pore networks, indicating that their fluid migration process is uneven, with three objective dominant connecting paths, which can affect the oil charging area and development efficiency.

## ■ ASSOCIATED CONTENT

### Data Availability Statement

Data analyses were conducted using Python scripts. The following open-source Python libraries were employed: umap-learn (v0.3.10), pandas (v1.5.3), gudhi (v3.8.0), numpy (v1.24.3), numba (v0.57.0), scipy (v1.10.1), scikit-learn (v1.3.0), and matplotlib (v3.7.1).

### Supporting Information

The Supporting Information is available free of charge at https://pubs.acs.org/doi/10.1021/acsomega.3c08847.

Pore distribution data by HIP and petrophysical properties of samples (PDF)

## ■ AUTHOR INFORMATION


### Corresponding Author

**Wei Wang** − *College of Chemistry and Chemical Engineering, Yulin University, Yulin 719000 Shaanxi, P. R. China;* orcid.org/0000-0001-7565-6969; Phone: +86 0912 3891144; Email: wangwei_1988@yulinu.edu.cn

### Authors

**Zhiyong Yan** − *No. 1 Oil Production Plant, Petrochina Changqing Oilfield Company, Yan'an 716000 Shaanxi, P. R. China*

**Lina Wang** − *No. 1 Oil Production Plant, Petrochina Changqing Oilfield Company, Yan'an 716000 Shaanxi, P. R. China*

**Shuang Xu** − *No. 1 Oil Production Plant, Petrochina Changqing Oilfield Company, Yan'an 716000 Shaanxi, P. R. China*

Complete contact information is available at: https://pubs.acs.org/10.1021/acsomega.3c08847


### Notes

The authors declare no competing financial interest.

## ■ ACKNOWLEDGMENTS

This research was financially supported by the National Natural Science Foundation of China (Nos. 41904128 and 42362023), the Department of Science and Technology of Shaanxi Province (Nos. 2023-JC-QN-0347 and 2024GX-YBXM-511), the Youth Innovation Team of Shaanxi Universities (23JP200), and Joint Fund of the Yulin University and the Dalian National Laboratory for Clean Energy (No. YLU-DNL Fund 2022012)

## ■ REFERENCES

(1) Ghanizadeh, A.; Clarkson, C.; Aquino, S.; Ardakani, O. H.; Sanei, H. Petrophysical and geomechanical characteristics of Canadian tight oil and liquid-rich gas reservoirs: II. Geomechanical property estimation. *Fuel* **2015**, *153* (1), 682−691.

(2) Li, Y.; Gao, X.; Meng, S.; Wu, P.; Niu, X.; Qiao, P.; Elsworth, D. Diagenetic sequences of continuously deposited tight sandstones in various environments: A case study from upper Paleozoic sandstones in the Linxing area, eastern Ordos basin, China. *AAPG Bull.* **2019**, *103* (11), 2757−2783.

(3) Wang, W.; Li, Y.; Chen, X. Microscope dynamic characterization of oil charging in tight sandstone using a physical simulation experiment. *J. Pet. Sci. Eng.* **2021**, *200*, 108379 DOI: 10.1016/j.petrol.2021.108379.

(4) Sun, Y.; Wei, Ln.; Dai, C. D.; Yu, Z.; Xin, Y. The carbonic acid-rock reaction in feldspar/dolomite-rich tightsand and its impact on CO2-water relative permeability during geological carbon storage. *Chem. Geol.* **2021**, *584*, No. 120527.

(5) Li, Y.; Wang, Z.; Pan, Z.; Niu, X.; Yu, Y.; Meng, S. Pore structure and its fractal dimensions of transitional shale: A cross-section from east margin of the Ordos Basin, China. *Fuel* **2019**, *241*, 417−431.

(6) Zhang, K. X.; Lai, J.; Bai, G. P.; Pang, X. J.; Ma, X. Q.; Qin, Z. Q.; Zhang, X. S.; Fan, X. C. Comparison of fractal models using NMR and CT analysis in low permeability sandstones. *Mar. Pet. Geol.* **2020**, *112*, No. 104069.

(7) Li, Y.; Yang, J.; Pan, Z.; Tong, W. Nanoscale pore structure and mechanical property analysis of coal: An insight combining AFM and SEM images. *Fuel* **2020**, *260*, 116352 DOI: 10.1016/j.fuel.2019.116352.

(8) Zhao, H.; Ning, Z.; Wang, Q.; Zhang, R.; Zhao, T.; Niu, T.; Zeng, Y. Petrophysical characterization of tight oil reservoirs using pressure-controlled porosimetry combined with rate-controlled porosimetry. *Fuel* **2015**, *154*, 233−242.

(9) Hazra, B.; Wood, D. A.; Kumar, S.; Saha, S.; Dutta, S.; Kumari, P.; Singh, A. K. Fractal Disposition and Porosity Characterization of Lower Permian Raniganj Basin Shales, India. *J. Nat. Gas Sci. Eng.* **2018**, *59*, 452−465, DOI: 10.1016/j.jngse.2018.09.014.

(10) Vishal, V.; Chandra, D.; Bahadur, J.; Sen, D.; Hazra, B.; Mahanta, B.; Mani, D. Interpreting Pore Dimensions in Gas Shales Using a Combination of SEM Imaging, Small-Angle Neutron Scattering, and Low-Pressure Gas Adsorption. *Energy Fuels* **2019**, *33* (6), 4835−4848.

(11) Wang, W.; Wang, R.; Wang, L.; Qu, Z.; Ding, X.; Gao, C.; Meng, W. Pore Structure and Fractal Characteristics of Tight Sandstones Based on Nuclear Magnetic Resonance: A Case Study in the Triassic Yanchang Formation of the Ordos Basin, China. *ACS Omega* **2023**, *8* (18), 16284−16297.

(12) Finkelstein, A.; Derdikman, D.; Rubin, A.; Foerster, J. N.; Las, L.; Ulanovsky, N. Three-dimensional head-direction coding in the bat brain. *Nature* **2015**, *517* (7533), 159−164.

(13) Otter, N.; Porter, M. A.; Tillmann, U.; Grindrod, P.; Harrington, H. A. A roadmap for the computation of persistent homology. *EPJ Data Sci.* **2017**, *6* (1), 1−38, DOI: 10.1140/epjds/s13688-017-0109-5.

(14) Gardner, R. J.; Hermansen, E.; Pachitariu, M.; Burak, Y.; Baas, N. A.; Dunn, B. A.; Moser, M.-B.; Moser, E. I. Toroidal topology of population activity in grid cells. *Nature* **2022**, *602* (7895), 123−128.

(15) Chaudhuri, R.; Gerek, B.; Pandey, B.; Peyrache, A.; Fiete, I. The intrinsic attractor manifold and population dynamics of a canonical cognitive circuit across waking and sleep. *Nat. Neurosci.* **2019**, *22* (9), 1512−1520, DOI: 10.1038/s41593-019-0460-x.

(16) Rybakken, E.; Baas, N.; Dunn, B. Decoding of Neural Data Using Cohomological Feature Extraction. *Neural Comput.* **2019**, *31* (1), 68−93.

(17) Townsend, J.; Micucci, C. P.; Hymel, J. H.; Maroulas, V.; Vogiatzis, K. D. Representation of molecular structures with persistent homology for machine learning applications in chemistry. *Nat. Commun.* **2020**, *11* (1), 3230 DOI: 10.1038/s41467-020-17035-5.

(18) Ismail, M. S.; Noorani, M. S. M.; Ismail, M.; Razak, F. A.; Alias, M. A. Early warning signals of financial crises using persistent homology. *Phys. A* **2022**, *586*, 126459 DOI: 10.1016/j.physa.2021.126459.

(19) Ishihara, S.; Franks, G.; Kano, J. Effect of particle packing structure on the elastic modulus of wet powder compacts analyzed by persistent homology. *Adv. Powder Technol.* **2023**, *34* (1), 103874 DOI: 10.1016/j.apt.2022.103874.

(20) Zulkepli, N. F. S.; Noorani, M. S.; Razak, F. A.; Ismail, M.; Alias, M. A. Hybridization of hierarchical clustering with persistent homology in assessing haze episodes between air quality monitoring stations. *J. Environ. Manage.* **2022**, *306*, 114434 DOI: 10.1016/j.jenvman.2022.114434.

(21) Mittal, K.; Gupta, S. Topological characterization and early detection of bifurcations and chaos in complex systems using persistent homology. *Chaos* **2017**, *27* (5), No. 051102, DOI: 10.1063/1.4983840.

(22) Ando, I.; Mugita, Y.; Hirayama, K.; Munetoh, S.; Aramaki, M.; Jiang, F.; Tsuji, T.; Takeuchi, A.; Uesugi, M.; Ozaki, Y. Elucidation of pore connection mechanism during ductile fracture of sintered pure iron by applying persistent homology to 4D images of pores: Role of open pore. *Mater. Sci. Eng.: A* **2021**, *828*, 142112 DOI: 10.1016/j.msea.2021.142112.

(23) Washburn, E.W. The Dynamics of Capillary Flow. *Phys. Rev.* **1921**, *17* (3), 273−283.

(24) Sussillo, D.; Barak, O. Opening the Black Box: Low-Dimensional Dynamics in High-Dimensional Recurrent Neural Networks. *Neural Comput.* **2013**, *25* (3), 626−649, DOI: 10.1162/NECO_a_00409. (acccessed 9/22/2023)

(25) Schmitz, S.; Weidner, U.; Hammer, H.; Thiele, A. Evaluating Uniform Manifold Approximation and Projection for Dimension Reduction and Visualization of Polinsar Features. *ISPRS Ann. Photogramm., Remote Sensing Spatial Inf. Sci.* **2021**, *V-1−2021*, 39−46, DOI: 10.5194/isprs-annals-V-1-2021-39-2021.

(26) McInnes, L.; Healy, J.; Melville, J. UMAP: Uniform Manifold Approximation and Projection for Dimension Reduction *arXiv preprint arXiv:1802.03426* 2018; Vol. *3* 29 DOI: 10.48550/arXiv.1802.03426.

(27) Rubin, A.; Sheintuch, L.; Brande-Eilat, N.; Pinchasof, O.; Rechavi, Y.; Geva, N.; Ziv, Y. Revealing neural correlates of behavior without behavioral measurements. *Nat. Commun.* **2019**, *10* (1), 4745 DOI: 10.1038/s41467-019-12724-2.

(28) Wang, W.; Li, W.; Xu, S. Classifications of the Reservoir Space of Tight Sandstone Based on Pore Structure, Connectivity, and Fractal Character: A Case Study from the Chang 7 Member of the Triassic Yanchang Formation in the Ordos Basin, China. *ACS Omega* **2022**, *7*, 10627−10637.

(29) Xiao, D.; Jiang, S.; Thul, D.; Lu, S.; Zhang, L.; Li, B. Impacts of clay on pore structure, storage and percolation of tight sandstones from the Songliao Basin, China: Implications for genetic classification of tight sandstone reservoirs. *Fuel* **2018**, *211* (1), 390−404.